Available online at www.sciencedirect.com
ScienceDirect
International Journal of Heat and Mass Transfer 51 (2008) 2519–2536
International Journal of HEAT and MASS TRANSFER
www.elsevier.com/locate/ijhmt

Numerical simulation of heat transfer and fluid flow past a rotating isothermal cylinder – A LBM approach

Y.Y. Yan *, Y.Q. Zu

School of the Built Environment, University of Nottingham, UK

Received 7 June 2006
Available online 31 October 2007

Abstract

In this paper, a viscous fluid flowing past a rotating isothermal cylinder with heat transfer is studied and simulated numerically by the lattice Boltzmann method (LBM). A numerical strategy for dealing with curved and moving boundaries of second-order accuracy for both velocity and temperature fields is proposed and presented. The numerical strategy and method are validated by comparing the present numerical results of flow without heat transfer with those of available previous theoretical, experimental and numerical studies, showing good agreements. On this basis, the convective heat transfer performance in such rotational boundary environments is further studied and validated; the numerical results are reported in the first time. The effects of the peripheral-to-translating-speed ratio, Reynolds number and Prandtl number on flow and heat transfer are discussed in details.

Keywords: Lattice Boltzmann method; Thermal lattice Boltzmann model; Rotating isothermal cylinder; Heat transfer; Boundary treatment

1. Introduction

Fluid flow around a rotating isothermal cylinder (or between two rotating cylinders) is a common occurrence in a variety of industrial processes. The operations can range from the contact cylinder dryers in the chemical process, food-processing, paper making and the textile industries to the cylindrical cooling devices in the glass and plastics industries. Although the configurations are normally rather simple, the flow past the rotating cylinder and the heat transfer performance between the fluid and the cylinder are very complex. Following factors involved in the flow, such as the features of viscous wakes including dissipation, diffusion and cancellation of the vortices, the effects of cylinder rotation on the production of lift force and moment, the local heat transfer performance around the cylindrical surface, and the evolution of surrounding temperature field with time, have greatly increased the difficulties to build up mathematical formulations and to simulate properly of such complex transport phenomena.

Over the past few decades, numerous theoretical, experimental and numerical efforts have been made to study isothermal flow fields past a rotating cylinder [1–7] or non-isothermal cross-flows over a fixed cylinder [8–12]. Unfortunately, the studies, especially the numerical simulations, on non-isothermal fluid flows past a rotating circular cylinder are still quite limited in spite of considerable technological interests. Early experimental studies on such flows were conducted by Peller et al. [13–15]. In their experiments, convective heat transfer from rotating and heated circular cylinders in cross flow and also the topological structure of boundary layers along the cylinder surface were measured at sub-critical free stream Reynolds number. The experiment performed by Özerdem [16] measured average convective heat transfer coefficients from a horizontal cylinder rotating in a quiescent air. Based on the experimental results, a correlation in terms of average Nusselt number and rotating Reynolds number has been established. However, it should be pointed out that, the overall or average Nusselt numbers determined by the above experiments

* Corresponding author. Tel.: +44 0 115 951 3168; fax: +44 0 115 951 3159.
E-mail address: yuying.yan@nottingham.ac.uk (Y.Y. Yan).

0017-9310/$ - see front matter © 2007 Elsevier Ltd. All rights reserved.
doi:10.1016/j.ijheatmasstransfer.2007.07.053

are only for a certain range of Reynolds number, it is still difficult to estimate instantaneously of the heat transfer contribution in each region of the rotating cylinder.

Kendoush [17] presented an approximate analytical model for calculating convective heat transfer over the surface of a rotating isothermal circular cylinder and an analytical correlation in which average Nusselt number is represented as a function of Reynolds and Prandtl numbers. However, the study did not consider the effect of cross-flow on heat transfer; the correlation is only valid for the heat transfer of a pure rotation of the cylinder. In general, the works of numerical modelling of convective heat transfer of rotating cylinders have not been well reported. A noted work [18] on this is of a numerical simulation based on the finite volume method (FVM) of convection around a heated rotating cylinder. In this modelling, the forced convection was purely caused by cylinder rotation; the effect of cross flow on heat transfer was not considered. In fact, the cylindrical coordinate used in this modelling has an inevitable weakness in treating boundaries as the outer boundary of the flow domain is a type of rectangle but not a circle with the same centre of the inner boundary. Therefore, it is necessary to carry out a further numerical study on convective heat transfer problems with cross-flow of rotating cylinders and meanwhile to overcome the above limitation of using FVM.

In the present study, a numerical approach to the performance of convective heat transfer across a heated rotating cylinder is achieved by applying the lattice Boltzmann method (LBM). Unlike conventional CFD simulations which are mainly based on direct numerical approximations to the macroscopic Navier–Stokes (N–S) and energy equations, the basic ideas of the LBM is to construct simplified kinetic models that incorporate the essential physics of microscopic or mesoscopic processes so that the macroscopic averaged properties can obey the desired macroscopic equations. The LBM has many computational advantages. To be different from macroscopic CFD methods which solve the N–S equations involving nonlinear convection terms, a LBM approach is based on solutions of lattice Boltzmann equations in which the advection operator is linear in the phase space. In addition, in macroscopic CFD methods, the pressure field is typically obtained by solving the Poisson or Poisson-like equations derived from incompressible N–S equations; this is normally of time consuming; whereas the pressure distributions can be obtained conveniently in the LBM by solving an extremely simple equation of state. Moreover, the inherent spatial locality of the updating rules makes the LBM to be more ideal for parallel computing. The other advantage of the LBM is that no-slip LBM boundary conditions cost little computational time. This makes the LBM to be very useful for simulating flow with complicated boundaries where efficient scheme for handling wall-fluid interaction is essential [19].

The existing LBM models for thermal fluid flow can basically be divided into two distinct categories. One is concerned with multi-speed models [20–22] which can particularly deal with density distribution function and introduce additional discrete velocities to obtain macroscopic energy equations and equilibrium distributions which usually include higher order velocity terms. The other category is concerned with multi-distribution function models [23–28], in which in addition to the original distribution function of density, a distribution function of temperature is also introduced. This type of models can overcome the limitation of multi-speed models and improve numerical instability [24]. Therefore, in the present study, a type of multi-distribution function model is integrated in the numerical scheme.

For the flow around a rotating circular cylinder, it is inevitable to deal with the velocity and temperature on curved boundaries. In the present LBM approach, an extrapolation method based on [29] is developed to handle the boundaries of temperature field. The method combined with the treatment of velocity boundary presented in [30] can indeed achieve second-order accuracy for both velocity and temperature on the curved wall. The present study will focus on the effects of peripheral-to-translating-speed ratio, Reynolds number and Prandtl number on the evolution of velocity and temperature fields around the cylinder and also the local and averaged heat transfer properties on the cylinder surface.

2. The LBM model

A two-dimensional nine-velocity (D2Q9) LBM model with multiple distribution functions is employed to simulate incompressible viscous thermal flows. A distribution function of temperature is used to calculate temperature field. While the macroscopic velocity and density fields are obtained by solving the distribution function of density.

2.1. Lattice Boltzmann equation of velocity field

The lattice Boltzmann equation of velocity field can be discretised in space $\mathbf{x}$ and time t into the following form:

$$f_\alpha(\mathbf{x}+\mathbf{e}_\alpha\delta t, t+\delta t) - f_\alpha(\mathbf{x},t) = -\frac{1}{\tau_v}[f_\alpha(\mathbf{x},t) - f_\alpha^{(\mathrm{eq})}(\mathbf{x},t)], \tag{1}$$

where $\mathbf{e}_\alpha(\alpha = 0,1,\ldots,8)$ is the particle velocity vector in the αth direction in the discrete velocity set of two-dimensional nine-velocity (D2Q9) model, as shown in Fig. 1; $f_\alpha(\mathbf{x},t)$ is a distribution function of density of the αth direction; $f_\alpha^{(\mathrm{eq})}(\mathbf{x},t)$ is its corresponding equilibrium state, τ_v is the dimensionless relaxation time of velocity field; and δt is the time step.

The equilibrium distribution function $f_\alpha^{(\mathrm{eq})}(\mathbf{x},t)$ in Eq. (1) is expressed as

$$f_\alpha^{(\mathrm{eq})}(\mathbf{x},t) = \omega_\alpha\rho\left[1 + \frac{3}{c^2}(\mathbf{e}_\alpha\cdot\mathbf{u}) + \frac{9}{2c^2}(\mathbf{e}_\alpha\cdot\mathbf{u})^2 - \frac{3}{2c^2}\mathbf{u}^2\right], \tag{2}$$

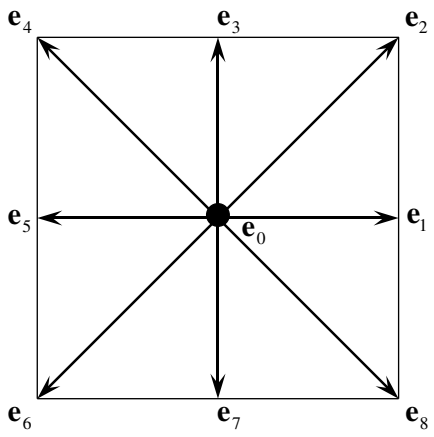

Fig. 1. Discrete velocity set of two-dimensional nine-velocity (D2Q9) model.

where $\mathbf{u}$ and ρ are the macroscopic velocity and density, respectively; the streaming speed, c, is defined as $c \equiv \delta x/\delta t$; where δx is the streaming length; ω_α is the weighting coefficient. In the D2Q9 model

$$\mathbf{e}_\alpha = \begin{cases} 0, & \alpha = 0, \\ (\cos[(\alpha-1)\pi/4], \sin[(\alpha-1)\pi/4])c, & \alpha = 1,3,5,7, \\ \sqrt{2}(\cos[(\alpha-1)\pi/4], \sin[(\alpha-1)\pi/4])c, & \alpha = 2,4,6,8, \end{cases} \tag{3}$$

$$\omega_\alpha = \begin{cases} 4/9, & \alpha = 0, \\ 1/9, & \alpha = 1,3,5,7, \\ 1/36, & \alpha = 2,4,6,8. \end{cases} \tag{4}$$

The sound speed in the model is represented as $c_s = c/\sqrt{3}$. The macroscopic quantities $\mathbf{u}$ and ρ are evaluated, respectively, as

$$\rho = \sum_\alpha f_\alpha \quad \text{and} \quad \rho\mathbf{u} = \sum_\alpha \mathbf{e}_\alpha f_\alpha. \tag{5}$$

According to the limit of incompressible flow, $Ma = |\mathbf{u}|/c_s \ll 1$ and the Chapman–Enskog expansion, the mass and momentum equations can be derived from the D2Q9 model as [31]

$$\nabla \cdot \mathbf{u} = 0, \tag{6}$$

$$\frac{\partial \mathbf{u}}{\partial t} + (\mathbf{u}\cdot\nabla)\mathbf{u} = -\frac{1}{\rho}\nabla p + \nu\nabla^2\mathbf{u}, \tag{7}$$

where the pressure p satisfies the equation of state as $p = \rho c_s^2$; the kinematical viscosity ν is determined by $\nu = (\tau_\nu - 0.5)/c_s^2\delta t$.

2.2. Lattice Boltzmann equation of temperature field

It is well accepted that the compression work carried out by pressure and viscous heat dissipation can be neglected in incompressible flow. On this basis, the lattice Boltzmann equation of temperature field can be given by

$$g_\alpha(\mathbf{x} + \mathbf{e}_\alpha\delta t, t + \delta t) - g_\alpha(\mathbf{x}, t) = -\frac{1}{\tau_c}[g_\alpha(\mathbf{x}, t) - g_\alpha^{(\mathrm{eq})}(\mathbf{x}, t)], \tag{8}$$

where τ_c is the dimensionless relaxation time; $g_\alpha(\boldsymbol{x}, t)$ is the temperature distribution function in the αth direction; $g_\alpha^{(\mathrm{eq})}(\boldsymbol{x}, t)$ is the corresponding equilibrium distribution function and can be expressed as [25,28]

$$g_\alpha^{(\mathrm{eq})}(\mathbf{x}, t) = \omega_\alpha T\left[1 + \frac{3}{c^2}\mathbf{e}_\alpha \cdot \mathbf{u}\right], \tag{9}$$

where T is the fluid temperature and can be evaluated from

$$T = \sum_\alpha g_\alpha. \tag{10}$$

In addition, it has been proved that the following macroscopic equation of temperature can be obtained from the Chapman–Enskog analysis as [25]:

$$\frac{\partial T}{\partial t} + \nabla\cdot(\mathbf{u}T) = \gamma\nabla^2 T, \tag{11}$$

where γ is the diffusivity coefficient which is represented as $\gamma = (\tau_c - 0.5)/c_s^2\delta t$.

In the LBM approach, both Eqs. (1) and (8) can be computed in two steps, namely, the collision and streaming steps. In the collision steps

$$\tilde{f}_\alpha(\mathbf{x}, t) = f_\alpha(\mathbf{x}, t) - \frac{1}{\tau_\nu}[f_\alpha(\mathbf{x}, t) - f_\alpha^{(\mathrm{eq})}(\mathbf{x}, t)] \tag{12a}$$

and

$$\tilde{g}_\alpha(\mathbf{x}, t) = g_\alpha(\mathbf{x}, t) - \frac{1}{\tau_c}[g_\alpha(\mathbf{x}, t) - g_\alpha^{(\mathrm{eq})}(\mathbf{x}, t)]. \tag{13a}$$

In the streaming steps

$$f_\alpha(\mathbf{x} + \mathbf{e}_\alpha\delta t, t + \delta t) = \tilde{f}_\alpha(\mathbf{x}, t) \tag{12b}$$

and

$$g_\alpha(\mathbf{x} + \mathbf{e}_\alpha\delta t, t + \delta t) = \tilde{g}_\alpha(\mathbf{x}, t), \tag{13b}$$

where $\tilde{f}_\alpha$ and $\tilde{g}_\alpha$ denote the post-collision states of the distribution function of density and distribution function of temperature, respectively. Obviously, the collision steps are completely local and the streaming processes take little computational effort at each time step, at which the distribution functions of a lattice are only affected by its neighbouring ones. This type of inherent spatial locality of the updating rules makes the LBM to be perfect for parallel computation.

3. Treatment for curved boundary

Fig. 2 shows an arbitrary curved wall (the dashed line) separating a solid region from fluid; where the black solid circles (●) denote intersections of the boundary with various lattice links ($\mathbf{x}_w$), the open circles (○) represent the boundary nodes in the fluid region ($\mathbf{x}_f$), and the grey solid circles (●) indicate those in the solid region ($\mathbf{x}_b$). Obviously,

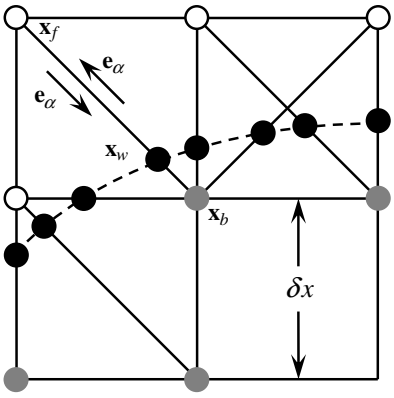

Fig. 2. Layout of the regularly spaced lattices and curved wall boundary.

both $\tilde{f}_\alpha(\mathbf{x}_b,t)$ and $\tilde{g}_\alpha(\mathbf{x}_b,t)$ are needed to perform the streaming steps on fluid nodes $\mathbf{x}_f$.

The fraction of an intersected link in the fluid region, Δ, is defined as

$$\Delta=\frac{|\mathbf{x}_f-\mathbf{x}_w|}{|\mathbf{x}_f-\mathbf{x}_b|}. \tag{14}$$

It is well known that a bounce-back boundary condition satisfies no-slip velocity boundary condition with a second-order accuracy if $\Delta=1/2$, so that a thermal boundary condition should be able to be implemented in a similar way to achieve the second-order accuracy. Certainly, this type of method can be used to treat simple boundaries of straight lines which are in parallel with the lattice grid. However, for a curved boundary, simply placing the boundary at $\Delta=1/2$ will factitiously change the geometry of the boundary and degrade the accuracy of the velocity and temperature fields. In the present study, a new method is proposed and introduced to deal with both velocity and temperature boundaries with second-order accuracy. For treating velocity field with curved boundaries, the method is based on the method reported in [30]; while for handling temperature fields with the curved boundaries, an extrapolation method of second-order accuracy is newly developed in the present study.

3.1. No-slip velocity boundary condition

Substantial evidence has shown that the bounce-back boundary conditions combined with interpolations including a one-half grid spacing correction at the boundaries are in fact of the second-order accuracy and thus capable of handling curved boundaries [30,31].

To construct the post-collision distribution function $\tilde{f}_{\bar{\alpha}}(\mathbf{x}_b,t)$ based upon the known information in the surroundings, a Chapman–Enskog expansion for the post-collision distribution function on the right-hand side of Eq. (12b) is conducted as

$$\tilde{f}_{\bar{\alpha}}(\mathbf{x}_b,t)=(1-\chi)\tilde{f}_\alpha(\mathbf{x}_f,t)+\chi f^*_\alpha(\mathbf{x}_b,t)+2\omega_\alpha\rho\frac{3}{c^2}\mathbf{e}_{\bar{\alpha}}\cdot\mathbf{u}_w, \tag{15}$$

where

$$f^*_\alpha(\mathbf{x}_b,t)=f^{(\mathrm{eq})}_\alpha(\mathbf{x}_f,t)+\omega_\alpha\rho(\mathbf{x}_f,t)\frac{3}{c^2}\mathbf{e}_\alpha\cdot(\mathbf{u}_{bf}-\mathbf{u}_f), \tag{16}$$

$$\mathbf{u}_{bf}=\mathbf{u}_{ff}=\mathbf{u}(\mathbf{x}_{ff},t),\ \chi=\frac{(2\Delta-1)}{(\tau-2)},\quad \text{if } 0\leqslant\Delta<\frac{1}{2}, \tag{17a}$$

$$\mathbf{u}_{bf}=\frac{1}{2\Delta}(2\Delta-3)\mathbf{u}_f+\frac{3}{2\Delta}\mathbf{u}_w,\quad \chi=\frac{(2\Delta-1)}{(\tau-1/2)},\quad \text{if } \frac{1}{2}\leqslant\Delta<1. \tag{17b}$$

In the above, $\mathbf{e}_{\bar{\alpha}}\equiv-\mathbf{e}_\alpha$; $\mathbf{x}_{ff}=\mathbf{x}_f+\mathbf{e}_{\bar{\alpha}}\delta t$; $\mathbf{u}_f\equiv\mathbf{u}(\mathbf{x}_f,t)$ is the fluid velocity near the wall; $\mathbf{u}_w\equiv\mathbf{u}(\mathbf{x}_w,t)$ is the velocity of solid wall; $\mathbf{u}_{bf}$ is the imaginary velocity for interpolations; and χ is the weight factor that depends on Δ. Substituting Eq. (16) into Eq. (15), gives

$$\tilde{f}_{\bar{\alpha}}(\mathbf{x}_b,t)=\tilde{f}_\alpha(\mathbf{x}_f,t)-\chi[\tilde{f}_\alpha(\mathbf{x}_f,t)-f^{(\mathrm{eq})}_\alpha(\mathbf{x}_f,t)]+\omega_\alpha\rho(\mathbf{x}_f,t)\frac{3}{c^2}\mathbf{e}_\alpha\cdot[\chi(\mathbf{u}_{bf}-\mathbf{u}_f)-2\mathbf{u}_w]. \tag{18}$$

It has been proved that a no-slip boundary condition of second-order accuracy can be achieved by this method [30].

3.2. Temperature boundary condition

To implement the curved boundary treatment for temperature, the nonequilibrium parts of temperature distribution function is introduced and defined as

$$g^{(\mathrm{neq})}_\alpha(\mathbf{x},t)=g_\alpha(\mathbf{x},t)-g^{(\mathrm{eq})}_\alpha(\mathbf{x},t). \tag{19}$$

Substituting Eq. (19) into Eq. (13a) leads to

$$\tilde{g}_\alpha(\mathbf{x},t)=g^{(\mathrm{eq})}_\alpha(\mathbf{x},t)+(1-\frac{1}{\tau_c})g^{(\mathrm{neq})}_\alpha(\mathbf{x},t). \tag{20}$$

Obviously, both $g^{(\mathrm{eq})}_{\bar{\alpha}}(\mathbf{x}_b,t)$ and $g^{(\mathrm{neq})}_{\bar{\alpha}}(\mathbf{x}_b,t)$ are required to determine the value of $\tilde{g}_{\bar{\alpha}}(\mathbf{x}_b,t)$.

It can be seen from Eq. (9) that $\mathbf{u}_b\equiv\mathbf{u}(\mathbf{x}_b,t)$ and $T_b\equiv T(\mathbf{x}_b,t)$ are necessary for the evaluation of $g^{(\mathrm{eq})}_{\bar{\alpha}}(\mathbf{x}_b,t)$.

Assuming that $\delta x=\delta t=\varepsilon$, then

$$\mathbf{u}_b=[\mathbf{u}_w+(\Delta-1)\mathbf{u}_f]/\Delta+\mathrm{O}(\varepsilon^2), \tag{21a}$$

$$\mathbf{u}_b=[2\mathbf{u}_w+(\Delta-1)\mathbf{u}_{ff}]/(1+\Delta)+\mathrm{O}(\varepsilon^2). \tag{21b}$$

Obviously, both $\mathbf{u}_{b1}=[\mathbf{u}_w+(\Delta-1)\mathbf{u}_f]/\Delta$ and $\mathbf{u}_{b2}=[2\mathbf{u}_w+(\Delta-1)\mathbf{u}_{ff}]/(1+\Delta)$ can be used to approximate $\mathbf{u}_b$ with second-order accuracy. Moreover, $\mathbf{u}_{b1}$ is usually more accurate than $\mathbf{u}_{b2}$ to be used to approximate $\mathbf{u}_b$ because $\mathbf{x}_f$ is closer to $\mathbf{x}_b$ than $\mathbf{x}_{ff}$. However, if Δ is small, $\mathbf{u}_{b1}$ will be too large and leads to the numerical instability in the simulation. Therefore, Δ is introduced as a weight, and $\mathbf{u}_b$ can be approximated by

$$\mathbf{u}^*_b=\mathbf{u}_{b1}\quad \text{if } \Delta\geqslant 0.75, \tag{22a}$$

$$\mathbf{u}^*_b=\Delta\mathbf{u}_{b1}+(1-\Delta)\mathbf{u}_{b2}\quad \text{if } \Delta<0.75. \tag{22b}$$

In a similar way, T_b can be approximated by

$$T^*_b=T_{b1},\quad \text{if } \Delta\geqslant 0.75, \tag{23a}$$

$$T^*_b=\Delta T_{b1}+(1-\Delta)T_{b2},\quad \text{if } \Delta<0.75, \tag{23b}$$

where $T_{b1} = [T_w + (\Delta - 1)T_f]/\Delta$, $T_{b2} = [2T_w + (\Delta - 1)T_{ff}]/(1 + \Delta)$; T_f and T_{ff} denote the temperature at $\mathbf{x}_f$ and $\mathbf{x}_{ff}$, respectively. For an arbitrary value of Δ, it can be easily proved that

$$\mathbf{u}_b = \mathbf{u}_b^* + \mathrm{O}(\varepsilon^2) \tag{24a}$$

and

$$T_b = T_b^* + \mathrm{O}(\varepsilon^2). \tag{24b}$$

By substitution of Eqs. (24a) and (24b), Eq. (9) becomes

$$g_{\bar{\alpha}}^{(\mathrm{eq})}(\mathbf{x}_b, t) = h_{\bar{\alpha}}^{(\mathrm{eq})}(\mathbf{x}_b, t) + \mathrm{O}(\varepsilon^2), \tag{25}$$

where

$$h_{\bar{\alpha}}^{(\mathrm{eq})}(\mathbf{x}_b, t) = \omega_{\bar{\alpha}} T_b^* \left[1 + \frac{3}{c^2}\mathbf{e}_{\bar{\alpha}} \cdot \mathbf{u}_b^*\right]. \tag{26}$$

The next task is to seek the second-order approximation for $g_{\bar{\alpha}}^{(\mathrm{neq})}(\boldsymbol{x}_b, t)$. Based on the Chapman–Enskog analysis, the solution for $g_\alpha(\boldsymbol{x}, t)$ can be expanded in the form of

$$g_\alpha(\mathbf{x}, t) = g_\alpha^{(0)}(\mathbf{x}, t) + \varepsilon g_\alpha^{(1)}(\mathbf{x}, t) + \mathrm{O}(\varepsilon^2). \tag{27}$$

where $g_\alpha^{(0)}(\mathbf{x}, t) = g_\alpha^{(\mathrm{eq})}(\mathbf{x}, t)$ is the equilibrium distribution function of temperature.

Similarly

$$g_\alpha(\mathbf{x} + \varepsilon\mathbf{e}_\alpha, t) = g_\alpha^{(0)}(\mathbf{x} + \varepsilon\mathbf{e}_\alpha, t) + \varepsilon g_\alpha^{(1)}(\mathbf{x} + \varepsilon\mathbf{e}_\alpha, t) + \mathrm{O}(\varepsilon^2). \tag{28}$$

Eq. (27) subtracted from Eq. (28) gives

$$g_\alpha^{(\mathrm{neq})}(\mathbf{x} + \varepsilon\mathbf{e}_\alpha, t) = g_\alpha^{(\mathrm{neq})}(\mathbf{x}, t) + \varepsilon[g_\alpha^{(1)}(\mathbf{x} + \varepsilon\mathbf{e}_\alpha, t) - g_\alpha^{(1)}(\mathbf{x}, t)] + \mathrm{O}(\varepsilon^2) \tag{29}$$

the Taylor series expansion for $g_\alpha^{(1)}(\mathbf{x} + \varepsilon\mathbf{e}_\alpha, t)$ at $(\mathbf{x}, t)$ results in

$$g_\alpha^{(1)}(\mathbf{x} + \varepsilon\mathbf{e}_\alpha, t) = g_\alpha^{(1)}(\mathbf{x}, t) + \varepsilon\mathbf{e}_\alpha \cdot \nabla g_\alpha^{(1)}(\mathbf{x}, t) + \mathrm{O}(\varepsilon^2). \tag{30}$$

Substituting Eq. (30) into Eq. (29) gives

$$g_\alpha^{(\mathrm{neq})}(\mathbf{x} + \varepsilon\mathbf{e}_\alpha, t) = g_\alpha^{(\mathrm{neq})}(\mathbf{x}, t) + \mathrm{O}(\varepsilon^2). \tag{31}$$

Thus

$$g_{\bar{\alpha}}^{(\mathrm{neq})}(\mathbf{x}_b, t) = g_{\bar{\alpha}}^{(\mathrm{neq})}(\mathbf{x}_f, t) + \mathrm{O}(\varepsilon^2). \tag{32}$$

By the same token, it can be proved that

$$g_{\bar{\alpha}}^{(\mathrm{neq})}(\mathbf{x}_b, t) = g_{\bar{\alpha}}^{(\mathrm{neq})}(\mathbf{x}_{ff}, t) + \mathrm{O}(\varepsilon^2). \tag{33}$$

Therefore, the distribution function, $h_{\bar{\alpha}}^{(\mathrm{neq})}(\mathbf{x}_b, t)$, can be used to approximate $g_{\bar{\alpha}}^{(\mathrm{neq})}(\mathbf{x}_b, t)$ as

$$h_{\bar{\alpha}}^{(\mathrm{neq})}(\mathbf{x}_b, t) = g_{\bar{\alpha}}^{(\mathrm{neq})}(\mathbf{x}_f, t), \quad \text{if } \Delta \geqslant 0.75, \tag{34a}$$

$$h_{\bar{\alpha}}^{(\mathrm{neq})}(\mathbf{x}_b, t) = \Delta g_{\bar{\alpha}}^{(\mathrm{neq})}(\mathbf{x}_f, t) + (1 - \Delta) g_{\bar{\alpha}}^{(\mathrm{neq})}(\mathbf{x}_{ff}, t), \quad \text{if } \Delta < 0.75. \tag{34b}$$

Obviously, for an arbitrary value Δ,

$$g_{\bar{\alpha}}^{(\mathrm{neq})}(\mathbf{x}_b, t) = h_{\bar{\alpha}}^{(\mathrm{neq})}(\mathbf{x}_b, t) + \mathrm{O}(\varepsilon^2). \tag{35}$$

Substituting Eqs. (25) and (35), Eq. (20) becomes

$$\tilde{g}_{\bar{\alpha}}(\mathbf{x}_b, t) = \tilde{h}_{\bar{\alpha}}(\mathbf{x}_b, t) + \mathrm{O}(\varepsilon^2), \tag{36}$$

where

$$\tilde{h}_{\bar{\alpha}}(\mathbf{x}_b, t) = h_{\bar{\alpha}}^{(\mathrm{eq})}(\mathbf{x}_b, t) + \left(1 - \frac{1}{\tau_c}\right) h_{\bar{\alpha}}^{(\mathrm{neq})}(\mathbf{x}_b, t). \tag{37}$$

Consequently, on temperature boundary, the second-order accuracy can be satisfied by using $\tilde{h}_{\bar{\alpha}}(\mathbf{x}_b, t)$ to approximate $\tilde{g}_{\bar{\alpha}}(\mathbf{x}_b, t)$.

3.3. Force evaluation

In the present simulation, the momentum-exchange method by Mei et al. [30] is employed to evaluate the force on a circular cylinder surface. In order to implement the method efficiently, a scalar array $\phi(i, j)$ is employed. $\phi(i, j) = 0$ if the lattice location (i, j) is occupied by fluid; $\phi(i, j) = 1$ is for those lattice nodes inside the solid body. For a given boundary node $\mathbf{x}_b$ inside the solid region, the momentum-exchange with all possible neighbouring fluid nodes over a time step is given by

$$\sum_{\alpha \neq 0} \mathbf{e}_\alpha [\tilde{f}_\alpha(\mathbf{x}_b, t) + \tilde{f}_{\bar{\alpha}}(\mathbf{x}_b + \mathbf{e}_{\bar{\alpha}}\delta t, t)][1 - \phi(\mathbf{x}_b + \mathbf{e}_{\bar{\alpha}}\delta t)]. \tag{38}$$

The total force acting on the solid wall by fluid can be obtained by summing the contribution over all boundary nodes $\mathbf{x}_b$ belonging to the body, namely,

$$\mathbf{F} = \sum_{\text{all } xb} \sum_{\alpha \neq 0} \mathbf{e}_\alpha [\tilde{f}_\alpha(\mathbf{x}_b, t) + \tilde{f}_{\bar{\alpha}}(\mathbf{x}_b + \mathbf{e}_{\bar{\alpha}}\delta t, t)][1 - \phi(\mathbf{x}_b + \mathbf{e}_{\bar{\alpha}}\delta t)]. \tag{39}$$

The force $\mathbf{F}$ is evaluated after the collision step; the value of $\tilde{f}_{\bar{\alpha}}$ at the boundary can be obtained by Eq. (18).

4. Numerical simulation

Fig. 3 shows the physical model of flow and heat transfer around a rotating isothermal circular cylinder of radius R. In a rectangular two-dimensional domain, the coordinates x and y are taken, respectively, to be measured along the horizontal and vertical directions with the origin at the centre of the circular cylinder. At the entrance, i.e. the left boundary, fluid with the constant temperature T_l is injected into the domain with constant uniform velocity U in x-direction. Meanwhile, a free outflow boundary with zero velocity and temperature gradients in x-direction is set at the right hand side boundary of the domain. The upper and lower boundaries which parallel to the x-axis are set as free-slip velocity and heat insulated boundaries. The above four boundaries of the flow field are placed far enough from the centre of the cylinder in order to eliminate the effect of the boundaries. In the present simulations, the boundaries at upstream and downstream are set, respectively, as 6.6 and 12.7 times of the radius away from the centre of the cylinder; the upper and lower walls are both set as 8.07 times of the radius away from the cylinder centre.

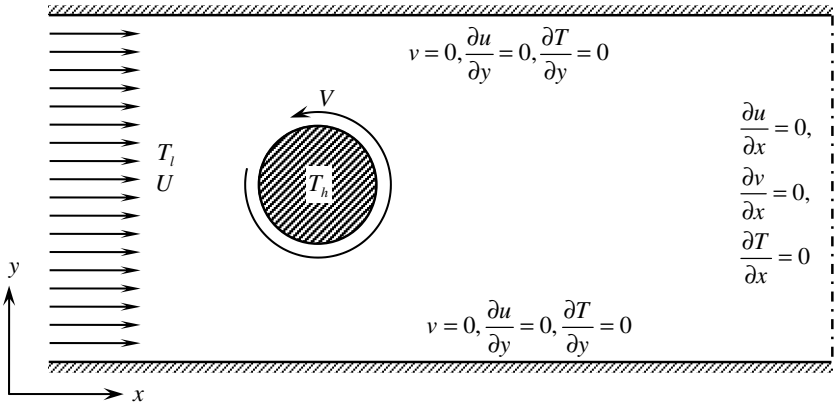

Fig. 3. Flow field set-up.

An initial field of flow is given by $u(x,y) = U$, $v(x,y) = 0$ with uniform temperature T_l, where u and v are, respectively, the x- and y-component of $\mathbf{u}$, and the cylinder is stationary with temperature T_h. At the next moment, the cylinder starts to rotate with an angular velocity Ω and the surface temperature remains to be constant as T_h.

The flow and heat transfer are simulated at $Re = 200$, 218, 500, and 1000, respectively; where the Reynolds number is defined as $Re = 2UR/v$. In order to regard the fluid as incompressible, the flow velocity must be much smaller than the speed of sound. Therefore, the inflow velocity U is set at 0.01 for $Re = 200$ and 218; 0.005 for $Re = 500$ and 1000, respectively. Parameter k is introduced to define the rate of the peripheral velocity $V = \Omega R$ to the inflow velocity U, i.e. $k = V/U$. Prandtl number at 0.1, 0.5, 0.71 and 1.0, respectively, is applied for each combination of k and Re; and for all cases of the simulation, $T_h = 40$, $T_l = 20$, $\rho = 6$ and $R = 15\delta x$ are used. Once U is determined, the kinetic viscosity v and thermal diffusivity γ are determined through Re and Pr; the peripheral velocity V is determined by parameter k.

To compare the current results with those from available previous studies, the following normalisations are conducted:

$$u^* = u/U, \quad v^* = v/U, \quad x^* = x/R, \quad y^* = y/R,$$
$$t^* = Ut/R, \quad T^* = \frac{T - T_l}{T_h - T_l}. \tag{40}$$

The drag and lift coefficients are defined as

$$\mathrm{CD} = \frac{D}{\rho U^2 R}, \quad \mathrm{CL} = \frac{L}{\rho U^2 R}, \tag{41}$$

where drag force D and lift force L are, respectively, the x-component and y-component of $\mathbf{F}$ given by Eq. (39).

The heat transfer convected from the cylindrical surface is estimated in terms of Nusselt number. Once the temperature field is determined, the following Nusselt numbers are defined, respectively, as

$$\text{local}: Nu = -\frac{2R}{(T_h - T_l)}\left(\frac{\partial T}{\partial \mathbf{n}}\right)_{\text{wall}}, \tag{42a}$$

$$\text{surface-averaged}: \langle Nu \rangle = \frac{1}{2\pi}\int_{-\pi}^{\pi} Nu \, \mathrm{d}\theta, \tag{42b}$$

$$\text{period-averaged}: \overline{Nu} = \frac{1}{t_p}\int_{t_p} Nu \, \mathrm{d}t, \tag{42c}$$

$$\text{and period-and-surface-averaged}: \overline{\langle Nu \rangle} = \frac{1}{t_p}\int_{t_p} \langle Nu \rangle \, \mathrm{d}t, \tag{42d}$$

where $\mathbf{n}$ is the outer-normal vector of cylindrical wall; angle θ equals zero at the rearmost point of the cylinder and increases in anticlockwise. The period-averaged quantities can only be calculated after the flow reaches the periodic state when the frequency of flow evolution, f, is obtained by a Fourier frequency analysis of the periodical variation of v at point $(9R, 0)$; and then the period is given by $t_p = 1/f$. Accordingly, the dimensionless frequency is defined by the following Strouhal number:

$$St = Rf/U. \tag{43}$$

5. Results and discussion

5.1. Velocity fields and the force acting on the cylinder

Velocity fields and the force acting on the cylinder are computed by the LBM and compared with the data available in literatures.

Fig. 4 shows the evolution of wake flow pattern at $Re = 200$, $k = 0.5$ for t^* from 1.0 to 13.0. The left column of the figure shows streamlines obtained by the present LBM and the right column shows experimental visualization pictures of Coutanceau and Menard [1]. The comparison between the LBM results and those from the experiment shows excellent agreement in terms of the formation of a Karman vortex street. Shu et al. have success-

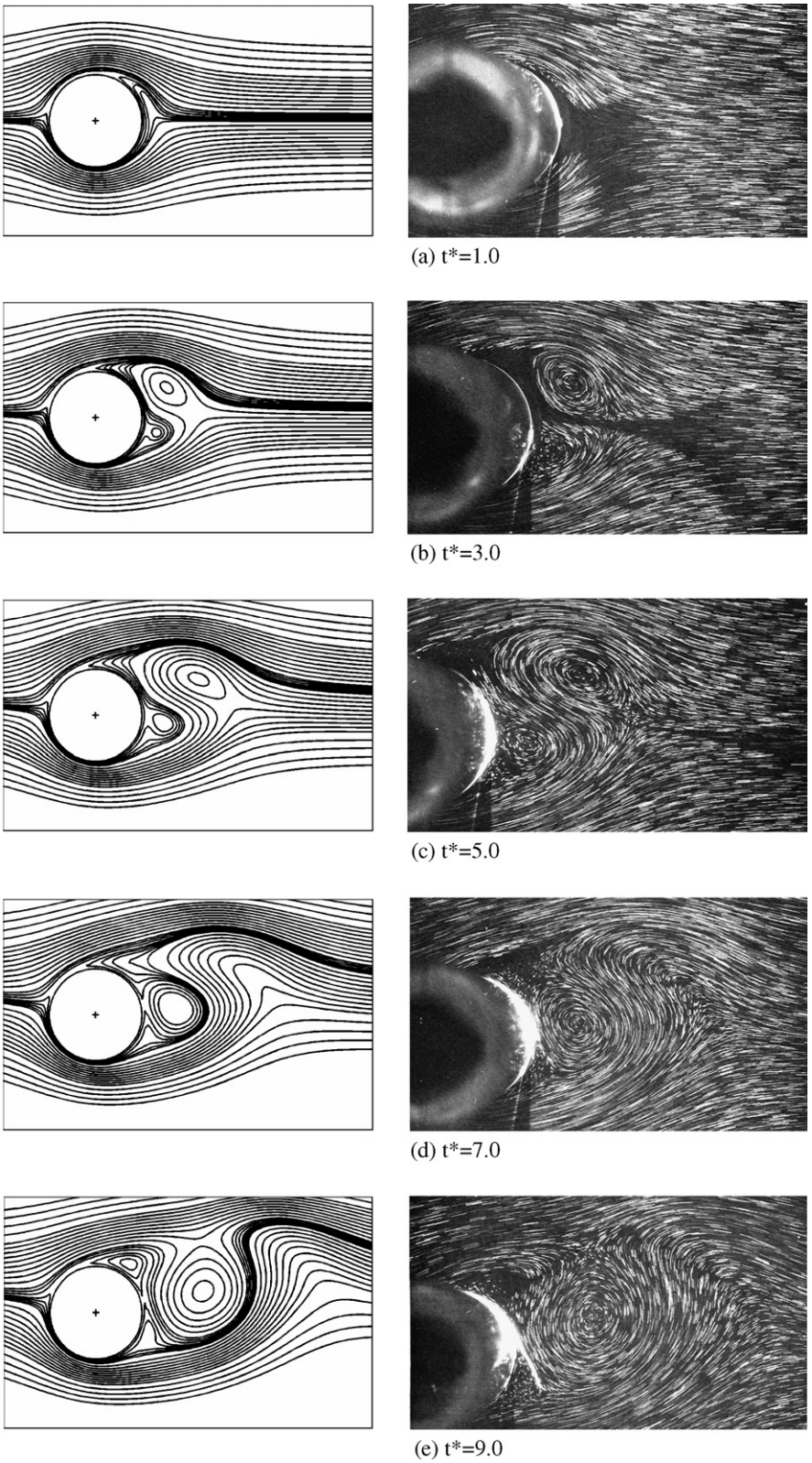

Fig. 4. Comparison between the evolution of the velocity field obtained by present computation and those by the experiment of Coutanceau and Menard [1] for $Re = 200$, $k = 0.5$ (left: obtained by present computation; right: obtained by experiment).

fully conducted a LBM simulation on the same problem of flow using the Taylor series expansion and least square method [7]. Fig. 5 shows a comparison of vorticity contours obtained by the present simulation and those reported by Shu et al. in [7]. Contour lines with positive (including zero) and negative vorticity values are shown

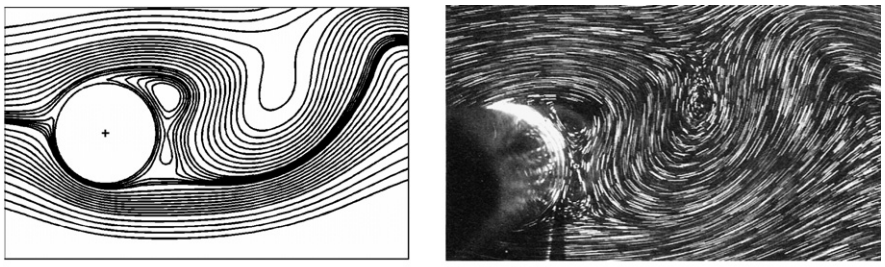

(f) t*=11.0

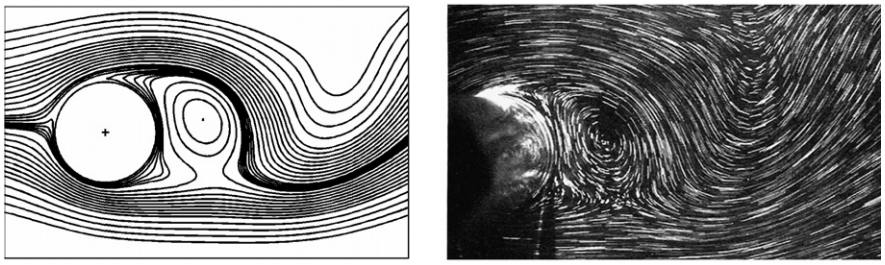

(g) t*=13.0

Fig. 4 (*continued*)

by solid and dashed lines, respectively. The comparison shows that the vorticity contours obtained by two different methods are quite consistent.

As a further check on consistency of the experimental and present numerical results, evolutions with time of u^* and v^* on positive x-axis are compared with the experimental results of Coutanceau and Menard [1]. Some representative points taken from the experimental study [1] are shown in Fig. 6 to illustrate the degree of the quantitative comparison.

The results of flow at $Re = 200$, $k = 1.0$ are presented in Figs. 7 and 8. In Fig. 7, the evolution of the velocity field obtained by the present calculation are shown and compared with those by Badr and Dennis [2] using the finite difference method (FDM). It is obvious that both calculations show similar streamlines except at $t^* = 6.0$ when, as

(a) t*=12.0

(b) t*=17.0

(c) t*=22.0

Fig. 5. Evolution of vorticity contours for $Re = 200$, $k = 1.0$. Contour lines with positive (including zero) and negative vorticity values are shown by solid and dashed lines, respectively. (left: obtained by present computation; right: obtained by Shu et al. [7] through TLLBM).

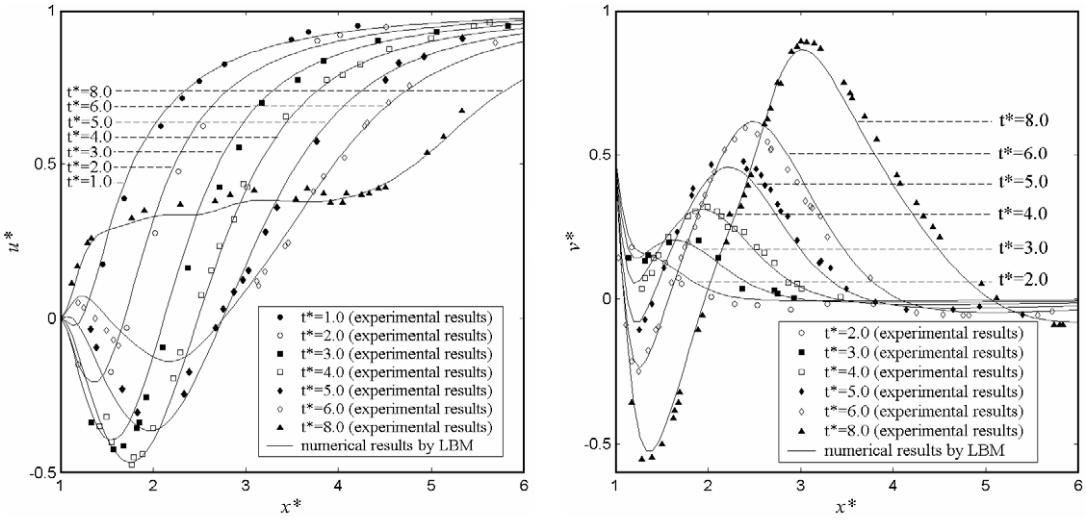

(a) u^* on the positive x-axis (b) v^* on the positive x-axis

Fig. 6. Time development of velocity profiles on x-axis for $Re = 200$, $k = 0.5$.

shown in Fig. 7d, the two vortices, which can be identified cleanly in the current LBM simulation, do not appear in the corresponding plot by the FDM. To justify which result is more accurate, the two numerical results at $t^* = 6.0$ are compared with the corresponding experimental result of Coutanceau and Menard [1] and shown in Fig. 8. It is clear that two vortices identified by the present LBM simulation are also observed by the experiment.

At $Re = 500$, the force acting on the rotating cylinder for $k = 0.1$, 0.5 and 1.0, respectively, is examined by the LBM. Numerical results of the variation of lift coefficient CL with time for different k is shown in Fig. 9a; obviously, the CL increases with t^* but decreases with k. In the same Figure, the numerical results are compared with the approximate analytical solution of Badr and Dennis [2]. The comparison indicates that the approximate analytical solution is suitable only in an early stage of flow evolution. The lift coefficients for $k = 0.5$ and 1.0 are also compared with the numerical results of Takada and Tsutahara [3], in which the evolution of isothermal flow around a suddenly rotating circular cylinder is simulated by two-dimensional seven-velocity (D2Q7) LBM model; the comparisons are presented in Fig. 9b. The lift coefficients obtained by the latter oscillate with large amplitude, especially at the early stage of the flow evolution. This kind of unphysical oscillation may be caused by the insufficient accuracy of the boundary definition. Since the boundary defined for the cylinder in [3] is not located on a pure circle but on a polygon, the cylinder must occupy much more lattice units to make the polygon to approach a circle. In fact, this kind of treatment has factitiously changed the real geometry of the boundary and therefore led to a reduction in the computational accuracy. The comparison in Fig. 9b shows that the present method for dealing with curved boundary can overcome the limitation mentioned above so that it is more accurate.

5.2. Temperature field

To evaluate the consistency of heat transfer between the present numerical prediction and according experimental measurement, the distribution of period-averaged Nusselt number on the surface of a stationary cylinder at $Re = 218$, $Pr = 0.71$ is calculated and compared with the experiments of Eckert and Soehngen [32]. As shown in Fig. 10, the distribution obtained by the present simulation agrees well with the experiment.

The current results are also validated by comparing with available numerical data for fixed or stationary cylinder, namely $k = 0$, such as the data by Momose and Kimoto [33] using the FDM. The comparison as shown in Fig. 11 indicates good agreement.

For heat transfer regarding flows across a rotating cylinder, due to the shortage of available experimental and numerical data from existing literatures, the present LBM results are compared with those of numerical calculations using in-house code of FVM [34] for the same problem at $Re = 200$, $Pr = 0.5$, $k = 0.5$. Fig. 12 shows the comparison of temperature distributions obtained by the two different methods. Obviously, the two results are consistent despite it is more inconvenient to deal with such type of rotating boundary conditions in the FVM.

Fig. 13 shows the evolution of temperature contours and corresponding velocity streamlines at $Re = 200$, $k = 0.5$, $Pr = 0.5$. It is noted that an impulsive start of the cylinder leads to a generation of initial thermal boundary layer near the surface of the isothermal cylinder, and moreover, the temperature contours almost parallel to the cylinder wall. As time marching, the thickness of the thermal boundary layer experiences a magnification. However, at the same time, the cross-flow conveys more and more heat from the front to the rear of the cylinder so that the extension of the thermal boundary layer is deeper at the rear than

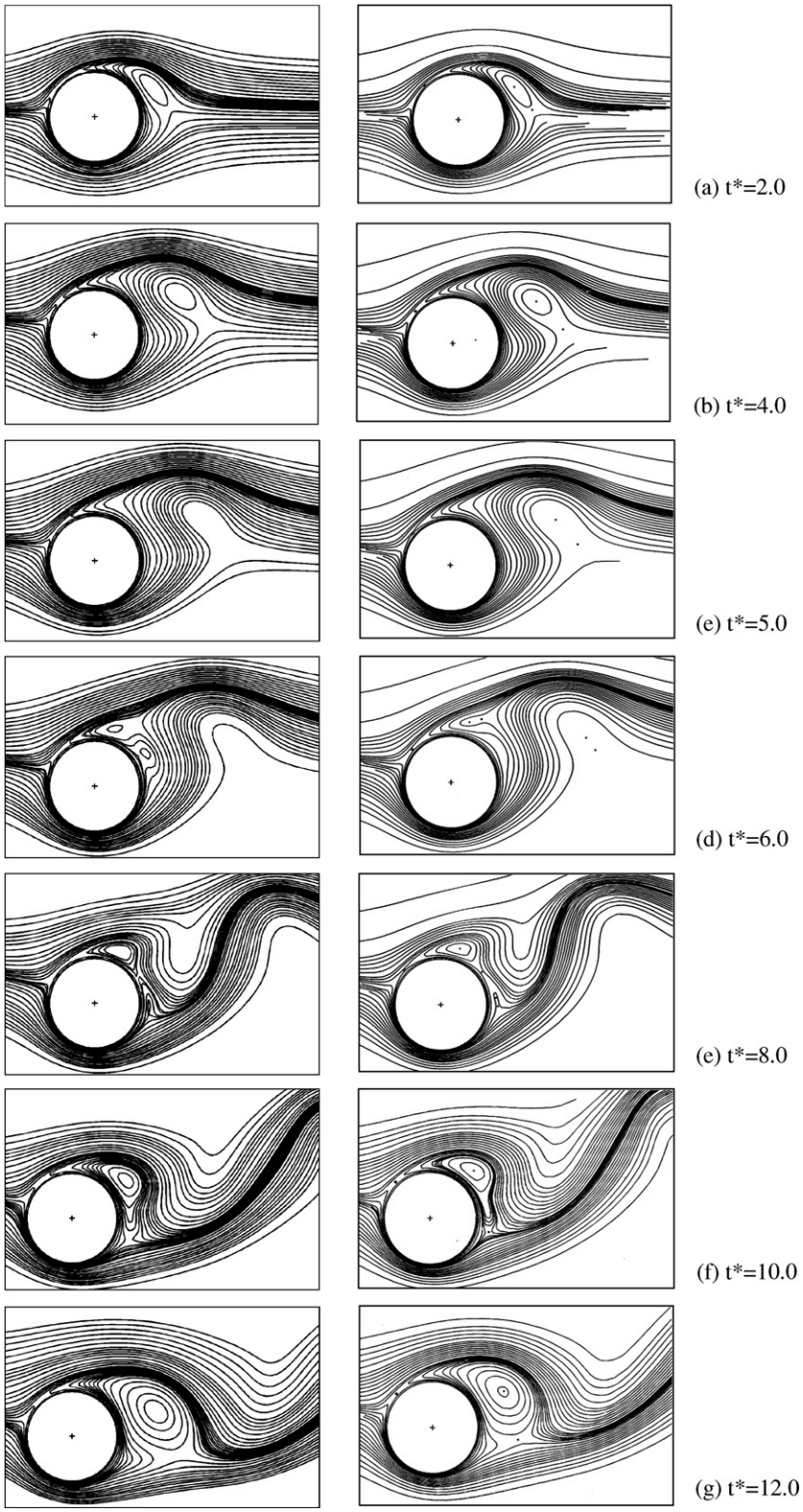

Fig. 7. Evolution of the velocity field for $Re = 200$, $k = 1.0$ (left: obtained by present computation; right: obtained by Badr and Dennis [2] through FDM).

it is in the front. This phenomenon becomes more evident with the time development. The warming up of the boundary layer at the rear of the cylinder results in a decrease of heat flux there. The numerical results also indicate that vortex shedding plays an important role in the heat transfer downstream. As shown in Fig. 13, with time marching, the vortices at the rear of the cylinder grow in size and ultimately detach into the wake while heat is carried away. As

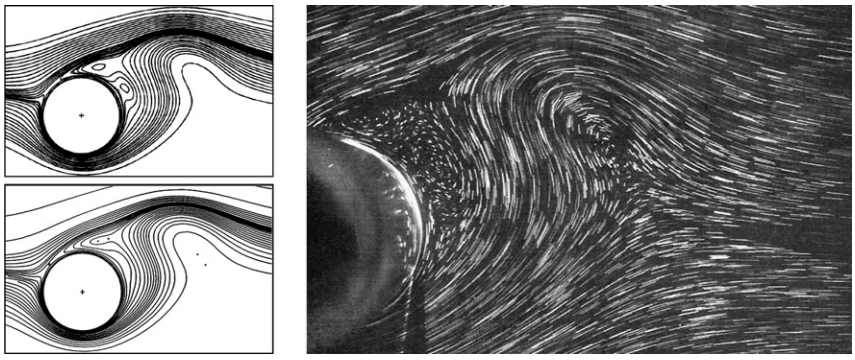

Fig. 8. Streamlines for $Re = 200$, $k = 0.5$ at $t^* = 6.0$ (top left: by LBM; lower left: by FDM; right: by experiment).

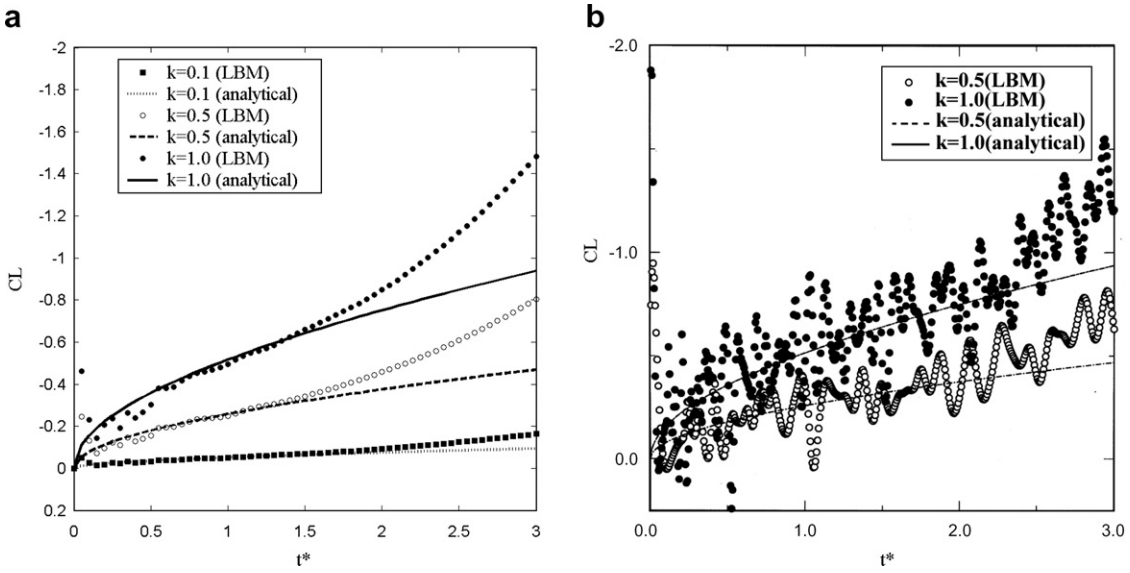

Fig. 9. The variation with time of the lift coefficient for $Re = 500$: (a) computed by present method; (b) computed by Takada and Tsutahara [3].

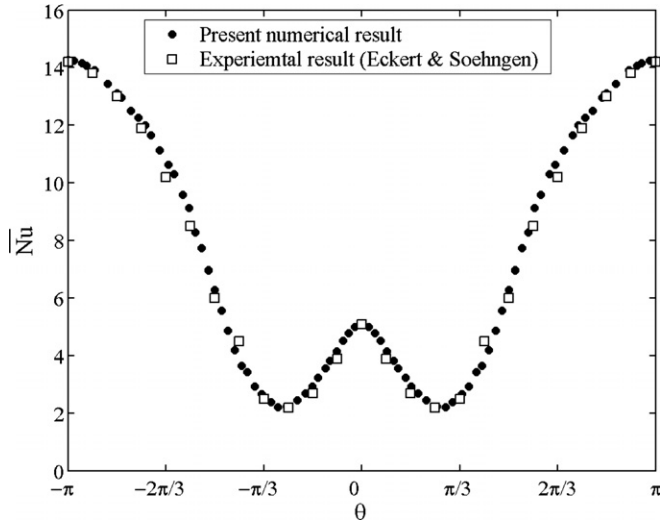

Fig. 10. Distribution of period-averaged Nusselt number on the cylinder surface at $Re = 218$, $Pr = 0.71$, $k = 0$.

a result, in the weak, high temperature concentrates in the regions where streamlines have large curvatures.

5.3. The effects of parameter k

The effects of parameter k on flow and heat transfer are predicted numerically. Figs. 14 and 15 show the early stage of temperature contour evolution and corresponding velocity streamlines at $k = 0$ and 0.1, $Re = 200$, $Pr = 0.5$, respectively.

In Fig. 14, the cylinder does not rotate as $k = 0$; two opposed symmetrical vortices are formed simultaneously because of the symmetry of the velocity gradient. The upper vortex rotates clockwise, and the lower vortex rotates anticlockwise. These two vortices grow in width and length with time, remain as symmetrical for a certain period of time and are stably attached to the cylinder. During this period, heat transfer also remains symmetry between the upper and lower part of the cylinder. After this, the vortices become asymmetrical and are shed alternately downstream, and meanwhile, the symmetry of heat transfer is destroyed.

When $k \neq 0$ (see Figs. 13 and 15), the velocity and temperature fields are quite similar to those for $k = 0$ at the start of cylinder rotation, but as t^* increases slightly,

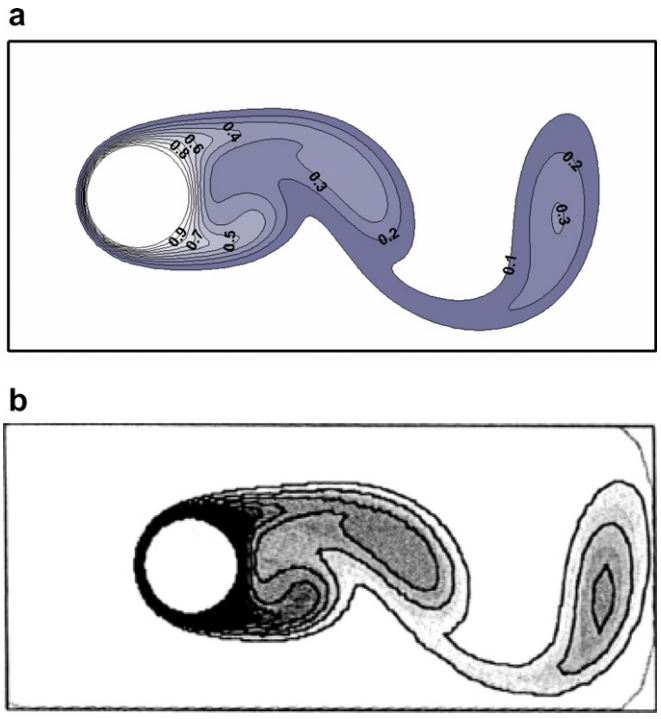

Fig. 11. Isothermal pattern at $Re = 200$, $Pr = 0.71$, $k = 0$, $t^* = 301.1$. (a) by LBM; (b) by FDM.

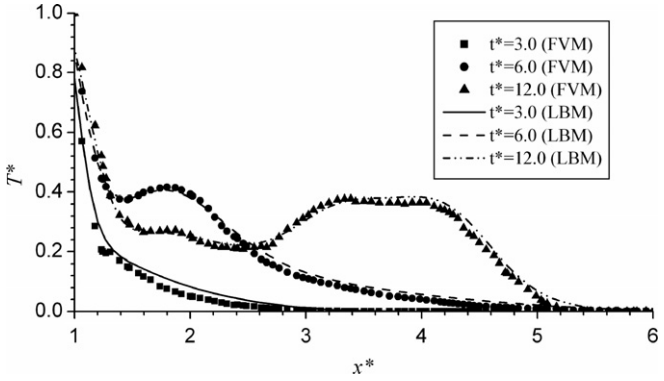

Fig. 12. Comparison of temperature distributions on x-axis obtained by LBM and FVM at $Re = 200$, $Pr = 0.5$, $k = 0.5$.

differences in the flow become obvious. The wall shear gradient becomes asymmetrical because the upper side of the cylinder moves against the free stream whereas the lower one moves in the direction of the free stream. As a result, the symmetry of the wall vorticity is destroyed and asymmetrical vortices appear. Moreover, the upper vortex appears earlier than that on the lower side. It can be identified by comparing the streamlines in Figs. 4 and 7 that the increase of parameter k inhibits the lower vortex formation. This has been verified by experiment in which the lower vortex becomes completely disappear when parameter $k > 2$ [1].

The other effect of parameter k on flow is to accelerate the detachment of vortices. For $k = 0$ (see Fig. 14) the vortices remain symmetrical and are stably attached to the cylinder when $t^* = 0$–16, whereas for $k = 0.1$, as shown in Fig. 15, the first vortex is completely shed downstream at $t^* = 16$; while, for $k = 0.5$, this happens more rapidly at $t^* = 6.0$. Indeed, this effect is very evident at the early stage of the flow and becomes weaker with the development of time.

The effect of k on Strouhal number and drag and lift coefficients is shown in Table 1. Strouhal number is calculated at $Re = 200$ after the flow reaches the periodic state. The results show that the Strouhal number rises slightly when parameter k increases from 0.1 to 1.0. The variation of the minimum, maximum and period-averaged values of drag and lift coefficients with k can be used to examine the effects of k on the forces acting on the surface of cylinder. Obviously, the period-averaged lift coefficients, $\overline{CL}$, for $k \neq 0$ are all less than zero since the anticlockwise rotation of the cylinder. Moreover, the increase of k from 0.1 to 1.0 results in the decrease of period-averaged drag coefficient, $\overline{CD}$, and the rise of the absolute value of $\overline{CL}$.

The variation of surface-averaged Nusselt numbers, $\langle Nu \rangle$, with time for different k are shown in Fig. 16; where the sub-graph at top right corner gives an enlarged view of the rectangular region enclosed by the dash-dotted lines. It is shown that surface-averaged Nusselt number for each case drops sharply in a short period after the flow started. Moreover, the highly consistent $\langle Nu \rangle - t^*$ curves indicate that the effect of rotation (or parameter k) on surface-averaged heat transfer is limited despite $\langle Nu \rangle$ decreases slightly with the increase of k.

The effect of k on local heat transfer coefficient is also predicted. The distributions of local Nusselt numbers at $Re = 200$, $Pr = 0.5$, $\theta \in [-\pi/2, \pi/2]$ for $k = 0.0$, 0.1 and 0.5 are shown in Fig. 17. It can be seen from the figure (a) that, for $k = 0$, the local Nu distribution is strictly symmetrical with respect to $\theta = 0$, and there are two local minimum values, noted as A and B, and a local maximum value noted as C. For convenience, the θ-components of point A, B and C are defined by θ_1, θ_2 and θ_3, respectively. Due to the symmetry nature, $\theta_1 = -\theta_2$ and $\theta_3 = 0$ in this case, the phenomenon may be connected with the fact that, for $k = 0$, the two vortices formed at the rear surface of the cylinder (see Fig. 14) rotate in opposite directions, roll up more and more heat from the upper and lower surfaces of the cylinder symmetrically while amplify the thickness of the thermal layers, and consequently diminish much more temperature gradient especially at the location of $\theta = \theta_1$ and $\theta = \theta_2$. Meanwhile, it can be noted in Fig. 14 that the rotating vortices form a narrow region along the positive x-axis, where u^* is negative. This region of reversed flow sweeps the thermal layers of lower temperature back to the cylinder surface and thus inhibits the reduction of temperature gradient there. As a result, a local maximum of Nusselt number appears at $\theta = \theta_3 = 0$. However, as shown in Fig. 17b and c, the symmetry of local Nusselt number distribution is destroyed by the unsymmetrical motion of vortices when $k \neq 0$. For example, for $k = 0.5$, the region with revised flow does not distribute along the x-axis but rocks up and down along

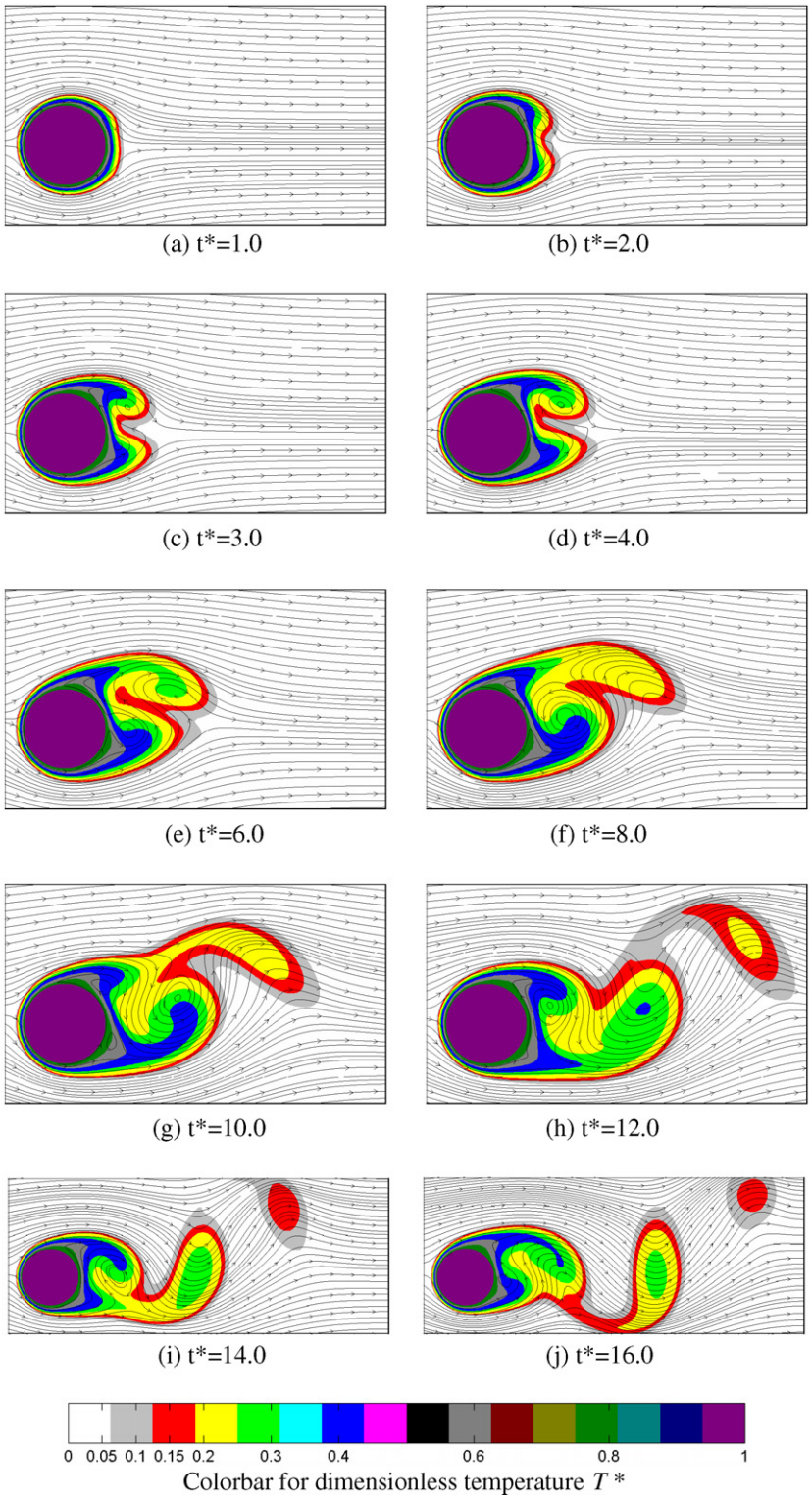

Fig. 13. Evolution of velocity streamlines and temperature contours for $Re = 200$, $k = 0.5$, $Pr = 0.5$.

with the migration and the alternative shedding of the vortices. Thus, the point A can not be kept at the location of $\theta = 0$. Moreover, the unsymmetrical motion of vortices results in $\theta_1 \neq -\theta_2$. Considering that the flow can reach a periodic state when t^* is large enough, the period-averaged values of Nusselt number distributions are calculated at $Re = 200$, $Pr = 0.5$ for different k and shown by Fig. 18. It can be seen clearly that the extreme values are tending to migrate along the surface of the cylinder anticlockwise with the increase of parameter k.

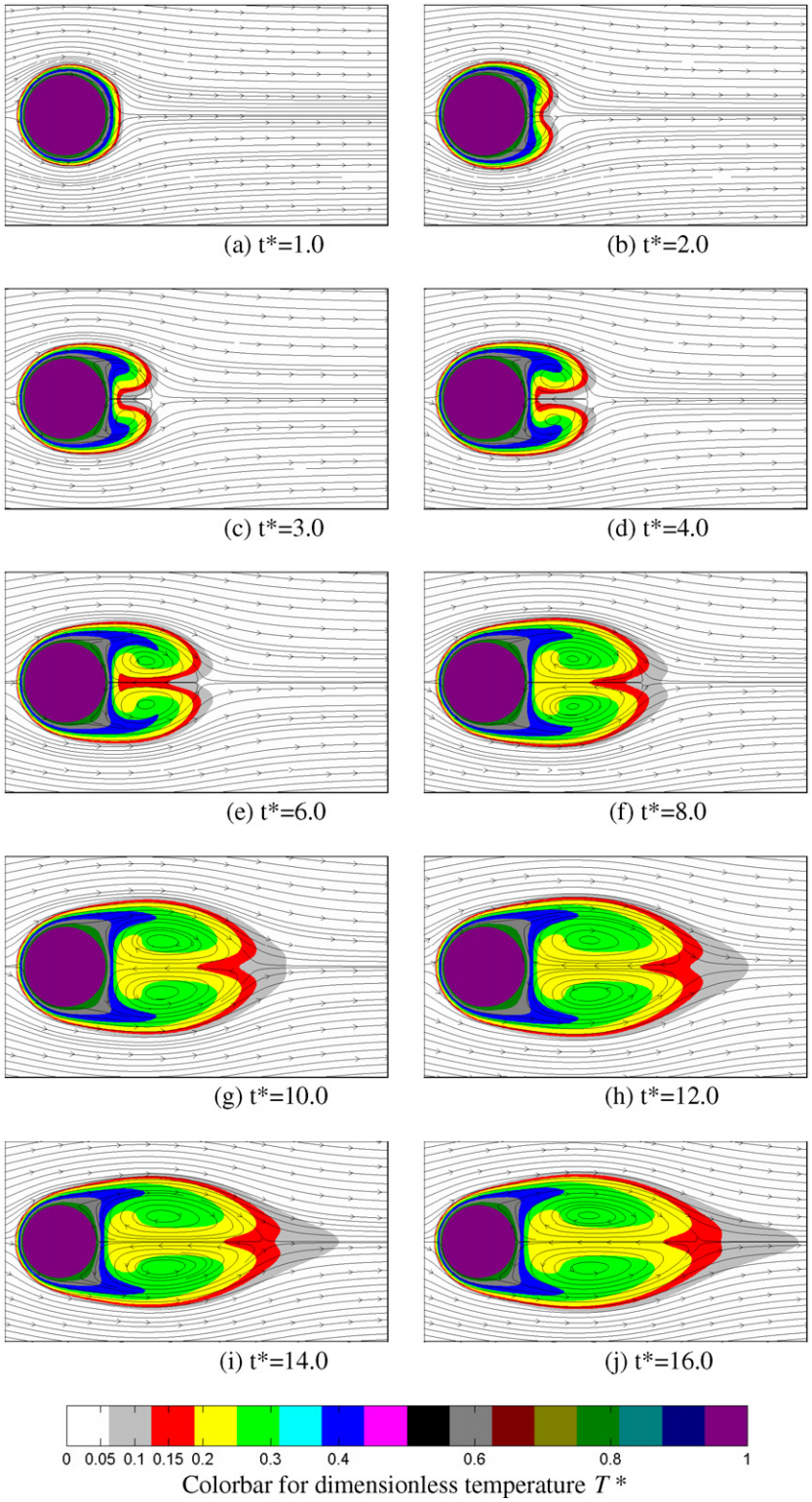

Fig. 14. Evolution of velocity streamlines and temperature contours for $Re = 200$, $k = 0$, $Pr = 0.5$.

To further examine the effect of reversed flow region, the local Nusselt number at $\theta = 0$ as a function of the time t^* and parameter k is shown in Fig. 19. Based on Fig. 19, the variation of Nu in three time intervals defined by S_1, S_2 and S_3, respectively, can be discussed. Within interval S_1, the vortices are either not formed or very weak, have little effect on the heat transfer. Some differences can be identified in S_2 if examining the corresponding streamline plots, as shown in Figs. 7, 13 and 14, that the vortices appearing in different cases grow up with the comparable speeds in

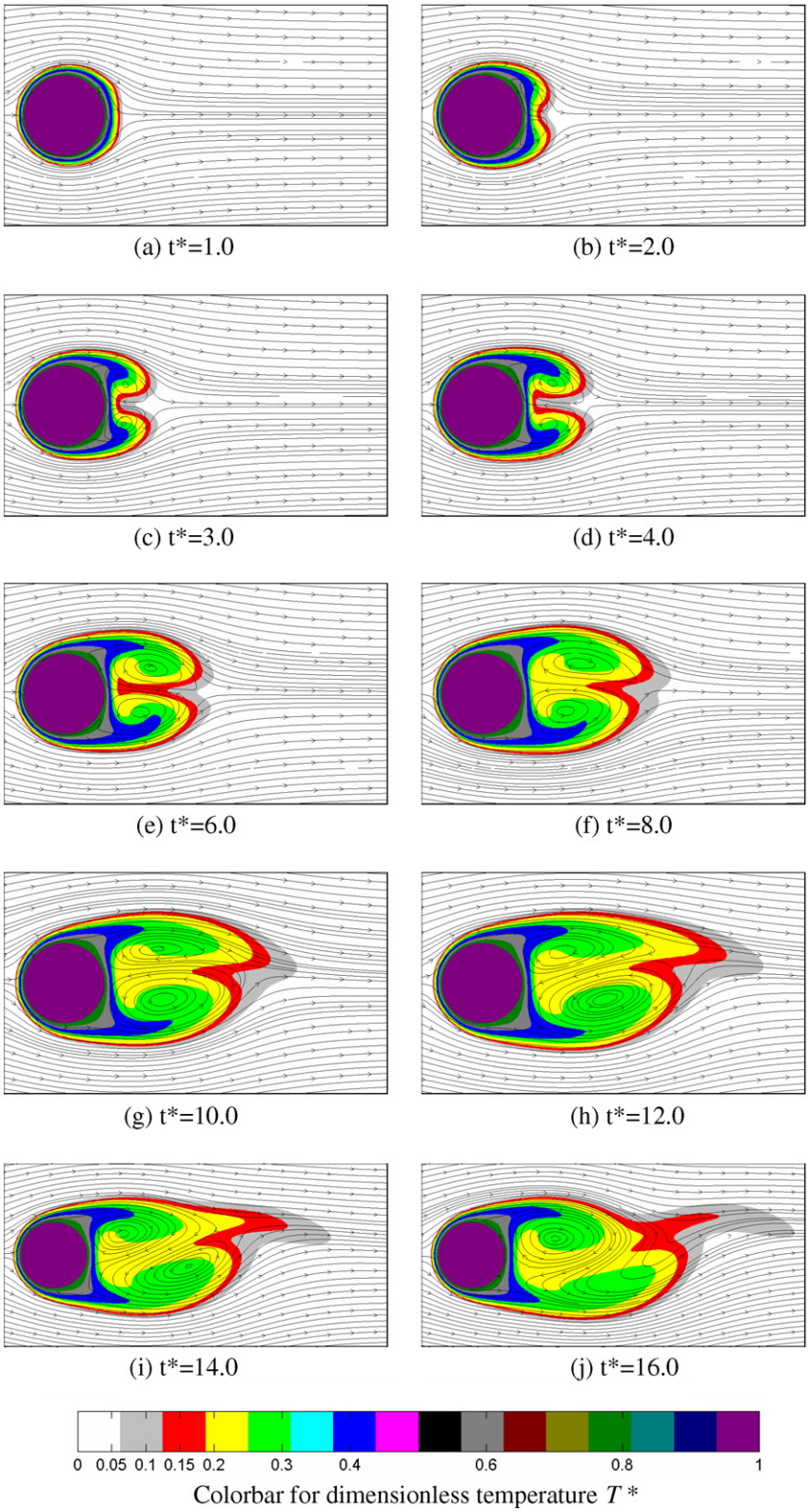

Fig. 15. Evolution of velocity streamlines and temperature contours for $Re = 200$, $k = 0.1$, $Pr = 0.5$.

this time interval, while the reversed flows are distinctly weakened with the increase of k; thus, it shows a climbing up for $k = 0$, a levelling off followed by descending for $k = 0.5$, and a steady decrease for $k = 1.0$. The development of Nu in S_3 is more variable. The enlargement of vortices for $k = 0$ continues and predominates over the effect of reversed flow to cause Nu a stable decrease. But, at the same time, the vortex shedding appears in the cases

Table 1
Strouhal number and drag and lift coefficients change with k at $Re = 200$

k	St	CD_{min}	CD_{max}	$\overline{CD}$	CL_{min}	CL_{max}	$\overline{CL}$
0.1	0.1089	1.432	1.680	1.553	−1.293	0.7746	−0.2669
0.5	0.1094	1.249	1.708	1.505	−2.365	−0.2838	−1.331
1.0	0.1100	0.9561	1.645	1.349	−3.706	−1.660	−2.699

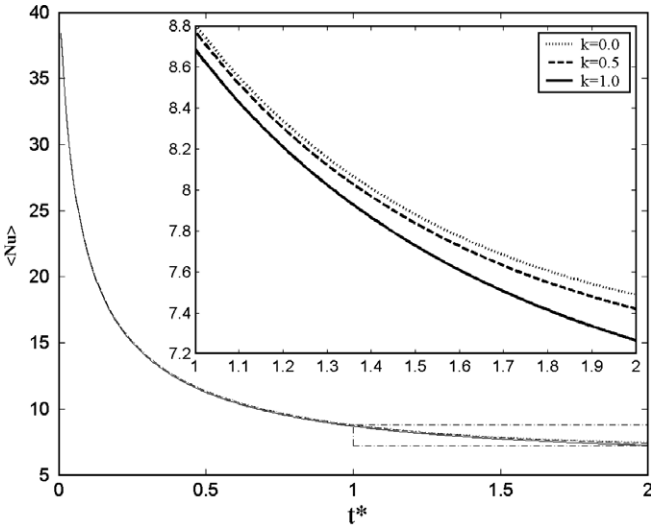

Fig. 16. Surface-averaged Nusselt numbers changes with k and t^*.

of $k = 0.5$ and 1.0 and interrupts the continuous growth of the vortices, which induces the reversed flow and vortices enlargement to dominate heat transfer at $\theta = 0$ alternatively. Thus, there are some fluctuations of the Nu values for $k = 0.5$ and 1.0 within S_3.

The development of surface-averaged Nusselt number with time at $Re = 200$, $k = 0.5$, $Pr = 0.5$ is shown in Fig. 20. It is indicated that the surface-averaged heat transfer coefficient can reach a periodic state when t^* is sufficient large. Thus, when $Re = 200$, the minimum, maximum and the period-averaged values of surface-averaged Nusselt

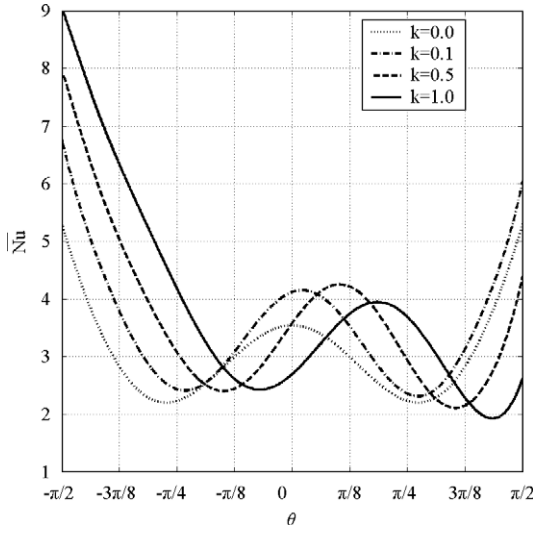

Fig. 18. Period-averaged Nusselt number along the cylinder surface at $Re = 200$, $Pr = 0.5$.

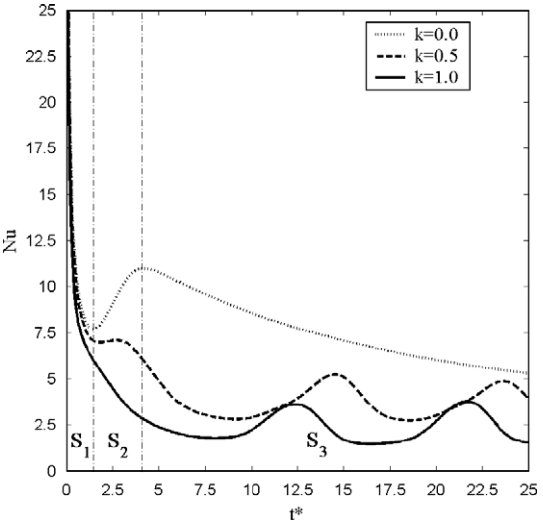

Fig. 19. Local Nusselt number changes with time and k at $\theta = 0$ for $Re = 200$, $Pr = 0.5$.

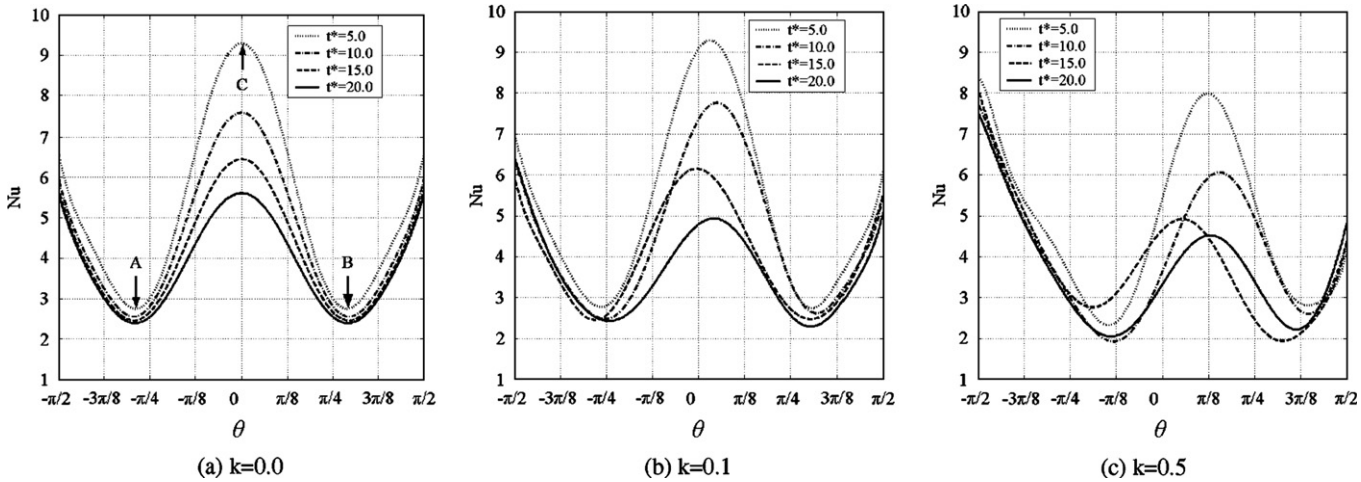

Fig. 17. Distributions of local Nusselt numbers for $Re = 200$, $Pr = 0.5$, $\theta \in [-\pi/2, \pi/2]$.

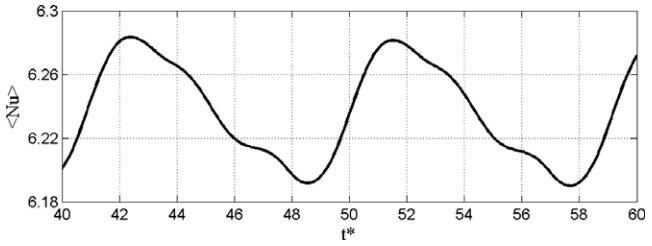

Fig. 20. Surface-averaged Nusselt number changes with time at $Re = 200$, $k = 0.5$, $Pr = 0.5$.

Table 2
Surface-averaged Nusselt number changes with k at $Re = 200$, $Pr = 0.5$ and 1.0

Pr	k	$\langle Nu\rangle_{min}$	$\langle Nu\rangle_{max}$	$\overline{\langle Nu\rangle}$
0.5	0.1	6.315	6.389	6.351
	0.5	6.190	6.283	6.237
	1.0	6.015	6.104	6.060
1.0	0.1	8.319	8.460	8.397
	0.5	8.048	8.246	8.167
	1.0	7.788	7.948	7.876

number, i.e. $\langle Nu\rangle_{min}$, $\langle Nu\rangle_{max}$ and $\overline{\langle Nu\rangle}$, at $Pr = 0.5$ and 1.0 for different k are further calculated; the results are shown in Table 2. The comparison of the data in Table 2 shows that the increase in parameter k can result in an evident decrease in $\langle Nu\rangle_{min}$, $\langle Nu\rangle_{max}$ and $\overline{\langle Nu\rangle}$.

5.4. The effects of Reynolds number and Prandtl number

Table 3 shows the effect of Reynolds number on Strouhal number and drag and lift coefficients. It is shown that Strouhal number and the period-averaged lift coefficient increase with Reynolds number, but the period-averaged drag coefficient decreases with Re. In Table 4, the minimum, maximum and period-averaged values of surface-averaged Nusselt number at different Re and Pr are given.

Table 3
Strouhal number and drag and lift coefficients change with Re for $k = 0.5$

Re	St	CD_{min}	CD_{max}	$\overline{CD}$	CL_{min}	CL_{max}	$\overline{CL}$
200	0.1094	1.249	1.708	1.505	−2.365	−0.2838	−1.331
500	0.1216	1.073	1.794	1.501	−2.656	−0.1238	−1.392
1000	0.1316	0.9724	1.759	1.419	−2.726	−0.2286	−1.491

Table 4
Variation of surface-averaged Nusselt number with Re and Pr for $k = 0.5$

Re	Pr	$\langle Nu\rangle_{min}$	$\langle Nu\rangle_{max}$	$\overline{\langle Nu\rangle}$
200	0.1	3.305	3.336	3.319
	0.5	6.190	6.283	6.237
	1.0	8.048	8.243	8.164
500	0.1	5.134	5.284	5.206
	0.5	9.726	10.42	10.11
	1.0	12.57	13.70	13.22
1000	0.1	7.147	7.562	7.303
	0.5	13.42	14.75	14.02
	1.0	16.88	18.44	17.6

It is clear that the surface-averaged Nusselt number increases with both Re and Pr.

6. Conclusion

A multi-distribution function LBM model for simulating viscous fluid flow past a rotating isothermal cylinder with heat transfer is presented. The model can deal with curved moving flow and thermal boundaries of second-order accuracy. The numerical results, such as velocity and temperature distributions and lift and drag coefficients, agree well with those reported in previous studies. The advantages of applying the LBM to such types of heat transfer problem can be effectively identified.

The effects of peripheral-to-translating-speed ratio k on flow and heat transfer are evaluated. Following conclusions in terms of an increase of k can be summarised:

(1) The formation of lower vortices is inhibited.
(2) Vortices shedding is greatly accelerated at the early stage of flow.
(3) The asymmetry distributions of velocity and temperature are enhanced.
(4) The extreme points of period-averaged Nusselt number migrate anticlockwise along the surface of cylinder.
(5) The period-and-surface-averaged Nusselt number is decreased.
(6) The absolute value of the lift coefficient is increased, but the drag coefficient is decreased.

The treatment for curved and moving boundary presented in this paper is simple and efficient. However, the calculation for the whole computational domain is relatively time consuming due to the application of uniform gird. The computation costs about 0.36 s per time-step on a Celeron 2.8 GHz PC machine with 1.00 GB of RAM. To improve the efficiency of computation, a stable LBM with non-uniform mesh should be proposed, which will be involved in our further work.

Acknowledgement

The work is partly supported by the UK EPSRC (Engineering Physical Science Research Council) under Grant EP/D500125/1.

References

[1] Madeleine Coutanceau, Christian Menard, Influence of rotation on the near-wake development behind an impulsively started circular cylinder, J. Fluid Mech. 158 (1985) 399–466.
[2] H.M. Badr, S.C.R. Dennis, Time-dependent viscous flow past an impulsively started rotating and translating circular cylinder, J. Fluid Mech. 158 (1985) 447–488.
[3] Naoki Takada, Michihisa Tsutahara, Evolution of viscous flow around a suddenly rotating circular cylinder in the lattice Boltzmann method, Comput. Fluids 27 (7) (1998) 807–828.

[4] Manoj T. Nair, Tapan K. Sengupta, Umendra S. Chauhan, Flow past rotating cylinders at high Reynolds numbers using higher order upwind scheme, Comput. Fluids 27 (1) (1998) 47–70.
[5] Sanjay Mittal, Bhaskar Kumar, Flow past a rotating cylinder, J. Fluid Mech. 476 (2003) 303–334.
[6] Michel Bergmann, Laurent Cordier, Jean-Pierre Brancher, On the generation of a reverse von Kármán street for the controlled cylinder wake in the laminar regime, Phys. Fluids 18 (2006) 1/028101–4/028101.
[7] C. Shu, K. Qu, X.D. Niu, Y.T. Chew, Numerical simulation of flows past a rotational circular cylinder by Taylor-series-expansion and Least Squares-based lattice Boltzmann Method, Int. J. Modern Phys. C 16 (11) (2005) 1753–1770.
[8] F. Dumouchel, J.C. Lecordier, P. Paranthoën, The effective Reynolds number of a heated cylinder, Int. J. Heat Mass Transfer 41 (12) (1998) 1787–1794.
[9] S. Sanitjai, R.J. Goldstein, Forced convection heat transfer from a circular cylinder in crossflow to air and liquids, Int. J. Heat Mass Transfer 47 (22) (2004) 4795–4805.
[10] J.-M. Shi, D. Gerlach, M. Breuer, G. Biswas, F. Durst, Heating effect on steady and unsteady horizontal laminar flow of air past a circular cylinder, Phys. Fluids 16 (12) (2004) 4331–4345.
[11] W.A. Khan, J.R. Culham, M.M. Yovanovich, Fluid flow around and heat transfer from an infinite circular cylinder, J. Heat Transfer 127 (7) (2005) 785–790.
[12] Takayuki Tsutsui, Tamotsu Igarashi, Heat transfer enhancement of a circular cylinder, J. Heat Transfer 128 (3) (2006) 226–233.
[13] H. Peller, V. Lippig, D. Straub, R. Waibel, Thermofluiddynamic experiments with a heated and rotating circular cylinder in crossflow. Part 1: Subcritical heat transfer measurements, Exp. Fluids 2 (3) (1984) 113–120.
[14] H. Peller, Thermofluiddynamic experiments with a heated and rotating circular cylinder in crossflow. Part 2.1: Boundary layer profiles and location of separation points, Exp. Fluids 4 (4) (1986) 223–231.
[15] H. Peller, D. Straub, Thermofluiddynamic experiments with a heated and rotating circular cylinder in crossflow. Part 2.2: Temperature boundary layer profiles, Exp. Fluids 6 (2) (1988) 111–114.
[16] Baris Özerdem, Measurement of convective heat transfer coefficient for a horizontal cylinder rotating in quiescent air, Int. Commun. Heat Mass Transfer 27 (3) (2000) 389–395.
[17] Abdullah Abbas Kendoush, An approximate solution of the convective heat transfer from an isothermal rotating cylinder, Int. J. Heat Fluid Flow 17 (4) (1996) 439–441.
[18] Rigoberto E.M. Morales, Augusto Balparda, Aristeu Silveira-Neto, Large-eddy simulation of the combined convection around a heated rotating cylinder, Int. J. Heat Mass Transfer 42 (5) (1999) 941–949.
[19] Shiyi Chen, Gary D. Doolen, Lattice Boltzmann method for fluid flows, Ann. Rev. Fluid Mech. 30 (1998) 329–364.
[20] F.J. Alexander, S. Chen, J.D. Sterling, Lattice Boltzmann thermohydrodynamics, Phys. Rev. E 47 (4) (1993) R2249–R2252.
[21] Chris Teixeira, Hudong Chen, David M. Freed, Multi-speed thermal lattice Boltzmann method stabilization via equilibrium under-relaxation, Comput. Phys. Commun. 129 (1/3) (2000) 207–226.
[22] Minoru Watari, Michihisa Tsutahara, Possibility of constructing a multispeed Bhatnagar-Gross-Krook thermal model of the lattice Boltzmann method, Phys. Rev. E 70 (2004) 1/016703–9/016703.
[23] Xiaowen Shan, Simulation of Rayleigh–Bénard convection using a lattice Boltzmann method, Phys. Rev. E 55 (1997) 2780–2788.
[24] Xiaoyi He, Shiyi Chen, Gary D. Doolen, A novel thermal model for the lattice Boltzmann method in incompressible limit, J. Comput. Phys. 146 (1) (1998) 282–300.
[25] Zhaoli Guo, Baochang Shi, Chuguang Zheng, A coupled lattice BGK model for the Boussinesq equations, Int. J. Numer. Methods Fluids 39 (4) (2002) 325–342.
[26] Y. Peng, C. Shu, Y.T. Chew, Simplified thermal lattice Boltzmann model for incompressible thermal flows, Phys. Rev. E 68 (2003) 1/026701–8/026701.
[27] Yong Shi, T.S. Zhao, Z.L. Guo, Thermal lattice Bhatnagar–Gross–Krook model for flows with viscous heat dissipation in the incompressible limit, Phys. Rev. E 70 (2004) 1/066310–10/066310.
[28] G. Barrios, R. Rechtman, J. Rojas, R. Tovar, The lattice Boltzmann equation for natural convection in a two-dimensional cavity with a partially heated wall, J. Fluid Mech. 522 (2005) 91–100.
[29] Zhaoli Guo, Chuguang Zheng, Baochang Shi, An extrapolation method for boundary conditions in lattice Boltzmann method, Phys. Fluids 14 (6) (2002) 2007–2010.
[30] Renwei Mei, Dazhi Yu, Wei Shyy, Li-Shi Luo, Force evaluation in the lattice Boltzmann method involving curved geometry, Phys. Rev. E 65 (2002) 1/041203–14/041203.
[31] Dazhi Yu, Renwei Mei, Li-Shi Luo, Wei Shyy, Viscous flow computations with the method of lattice Boltzmann equation, Prog. Aerosp. Sci. 39 (5) (2003) 329–367.
[32] E.R.G. Eckert, E. Soehngen, Distribution of heat transfer coefficients around circular cylinders in cross-flow at Reynolds numbers from 20 to 500, Trans. ASME 74 (3) (1952) 343–347.
[33] K. Momose, H. Kimoto, Forced convection heat transfer from a heated circular cylinder with arbitrary surface temperature distributions, Heat Transfer – Asian Res. 28 (6) (1999) 484–499.
[34] H. Lai, Y.Y. Yan, The effect of choosing dependent variables and cell-face velocities on convergence of the SIMPLE algorithm using non-orthogonal grids, Int. J. Numer. Methods Heat Fluid Flow 11 (5/6) (2001) 524–546.